Sheffield Hallam University

Effect of short-term low-temperature austempering on the microstructure and abrasive wear of medium-carbon low-alloy steel

LUO, Quanshun <http://orcid.org/0000-0003-4102-2129>, MEI, Haijuan, KITCHEN, Matthew, GAO, Yubi and BOWEN, Leon

Citation:

Copyright and re-use policy

Effect of Short-Term Low-Temperature Austempering on the Microstructure and Abrasive Wear of Medium-Carbon Low-Alloy Steel

Quanshun Luo[1] · Haijuan Mei[2] · Matthew Kitchen[1] · Yubi Gao[3] · Leon Bowen[4]

Abstract

Nano-bainitic steels have attracted great attention for good wear resistance. In this research, a medium-carbon low-alloyed steel was austempered at a low temperature close to its martensite-start temperature for various times to obtain mixed microstructure of nano-bainite, martensite and retained austenite. The austempered samples were characterised comprehensively by field-emission SEM and quantitative XRD. Its two-body abrasive wear property was evaluated by sliding on a SiC abrasive disc. The results revealed the formation of initial nano-width carbide-free bainitic ferrite (BF) after austempering by 10 min, whereas the BF size and amount both increased with the austempering time. The austempered samples exhibited wear coefficients lower than the quenched martensitic sample by up to 50%. SEM and TEM observations showed wear mechanisms of micro-cutting and ploughing deformation, including the formation of a nano-laminate top layer and bending deformation in the subsurface multiphase microstructure. The decreased wear loss was attributed to the role of retained austenite in the increased plasticity.

Keywords Low-temperature austempering · Bainite transformation · Trained austenite · Carbon partitioning · Abrasive wear

1 Introduction

Medium-carbon martensitic and bainitic steels are widely used wear resistant materials [1–3]. The wear behaviour of martensitic and bainitic steels, depending on the applied wear modes, relies strongly on the hardness and toughness properties as well as the strain hardening behaviour. These properties are closely related to the amount and stability of retained austenite and the carbon supersaturation in martensitic and bainitic ferrites. A novel heat treatment, called quenching–partitioning (Q–P) or quenching–partitioning–tempering (Q–P–T) [4–6], has been introduced to enhance the strength and toughness properties. Lower bainite is another type of hardened structure of medium-carbon steels [7–9]. More recently, a new process to get ultrahigh hardness and strength properties of high-carbon Si-alloyed steels has emerged by allowing the bainite transformation at even lower temperature. The resultant microstructure comprises finer sized carbide-free bainitic ferrite (BF) laths and inter-lath filmy austenite [10–14].

A recent comparative study of low carbon and Si-Mn alloyed steel 20Si2Mn3 revealed superior wear resistance of the Q–P–T treated samples to the conventionally quenching–tempering (Q–T) hardened sample, for the enriched amount of retained austenite was found to bring about a transition of the major wear mechanism from micro-cutting to ploughing and plastic fatigue wear [15]. Other researchers have also reported the benefits of increased austenite in promoting work hardening of worn surfaces through straining induced martensite transformation and high dislocation density [16–25]. Owing to these wear mechanisms,

✉ Quanshun Luo
q.luo@shu.ac.uk

1 Materials and Engineering Research Institute, Sheffield Hallam University, Sheffield S1 1WB, UK

2 School of Electromechanical Engineering, Guangdong University of Technology, Guangzhou 510006, Guangdong Province, China

3 State Key Laboratory of Advanced Processing and Recycling of Nonferrous Metals, Lanzhou University of Technology, Lanzhou 730050, Gansu Province, China

4 Department of Physics, Durham University, Durham DH1 3LE, UK

austenite-enriched bainitic steels were reported to be superior to martensitic steels in the wear under severe loading conditions [17–21]. Meanwhile, pearlite, bainite and martensite structures of similar hardness showed different wear property and wear mechanisms under the same abrasive wear conditions [21–23]. So far, the published work has indicated great potential of better wear resistance through microstructure control.

Short-term austempering is a hardening treatment intermediate between conventional bainitic austempering and martensitic quenching, which results in multi-constituent structure of martensite, bainite and austenite [26–28]. The strengthening mechanisms of the multi-constituent structure have been described to include hardening of martensite due to carbon enrichment, strain-hardening of bainite, refining of martensite due to pre-formed bainite, as well as the increased retained austenite [3, 28]. The improved strength and toughness properties have shown influence on the wear behaviour [13, 18, 20–24].

In this paper, we present experimental investigation of the abrasive wear property and wear mechanisms with a special attention on the role of nanobainite and retained austenite. For this purpose, a candidate steel having a medium carbon content and sufficient hardenability was austempered at a temperature close to its Ms point for various times to obtained multiphase microstructure of carbide-free BF, martensite and retained austenite. The austempering treatment was found to be beneficial to the two-body abrasive wear property as compared to the conventional quenching treatment.

2 Experimental

In selecting the sample steel, we have considered its medium carbon content to represent some mostly used wear resistant steels as shown in Refs [1–3]. In addition, the type and quantity of alloying elements should meet the requirement of hardenability, i.e., prevention of eutectoid pearlite transformation of under-cooled austenite in the applied austempering treatments. For this purpose, we selected a medium-carbon and Si-Mn-Ni–Cr-Mo-V alloyed steel grade, 300 M, having chemical compositions (in wt%) of C 0.42, Mn 0.75, Si 1.65, Ni 0.80, Cr 0.80, Mo 0.40, V 0.07, and Fe in balance. Its martensite-starting (Ms) temperature is 285 °C [29]. The steel was provided as a hot rolled and annealed bar of 32 mm in diameter, from which samples for this work were cut as 8 mm thick coupons. Two electrical resistant furnaces were employed to carry out the austempering heat treatments, as schematically shown in Fig. 1. The samples were loaded to the first furnace and heated from room temperature (23 °C) to 900 °C, whereas the second furnace was held at a fixed temperature of 285 °C. After holding in
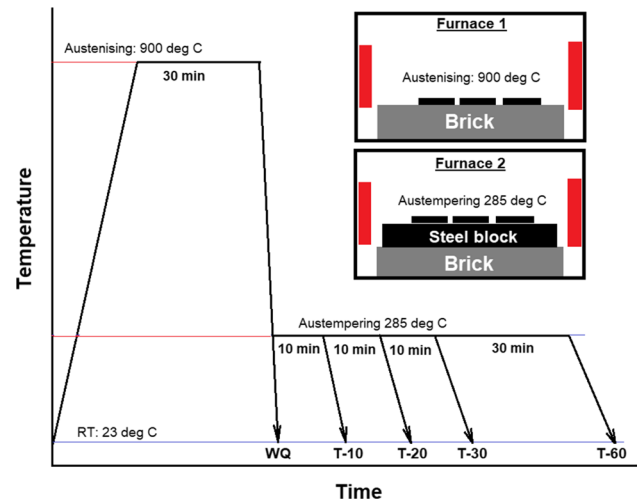

Fig. 1 The austempering and quenching treatments applied in this work

the first furnace for 30 min, one coupon was quenched in water, i.e., the sample WQ, and the rest four coupons were immediately moved to the second furnace for the isothermal austempering. The austempering times were 10, 20, 30 and 60 min respectively before air cooling to room temperature, i.e., the samples T-10, T-20, T-30 and T-60.

After the heat treatments, the samples were cut as rectangular blocks 4 mm × 8 mm × 25 mm using a thin SiC abrasive cutting wheel under water based cooling. Vickers hardness tests were undertaken at loads of 30 kg and 0.1 kg respectively. The average hardness and deviation were calculated from five indents.

A tribometer (CERT-UMT-2) was employed to perform two-body abrasive wear. The multi-functional tribometer enables two-dimensional reciprocating sliding with computer-programmed speed control. Figure 2a shows the test configuration, where a pin sample is fixed in a vertically aligned holder. The pin performs reciprocating sliding wear against a horizontally-aligned abrasive disc. The applied abrasive disc was made from SiC particles bonded in thermoset resin. Figure 2b shows a polished section of the SiC disc, in which the SiC abrasives exhibit multi-facet sharp angular shape. The SiC abrasive size was measured to be 124 ± 36 μm.

Reciprocating sliding was provided in the forward–backward direction at a nominal speed 50 mm/s, sliding length 30 mm, and testing time 20 min. Meanwhile, the pin sample also performed slow reciprocating sliding at the left–right direction at a nominal linear speed 0.1 mm/s and a fixed length 40 mm. The applied normal load was 5 N. A high-precision balance (0.1 mg) was used to measure the mass loss, which was then converted to volume loss by assuming the steel density 7.8 g cm^3. The wear coefficient was
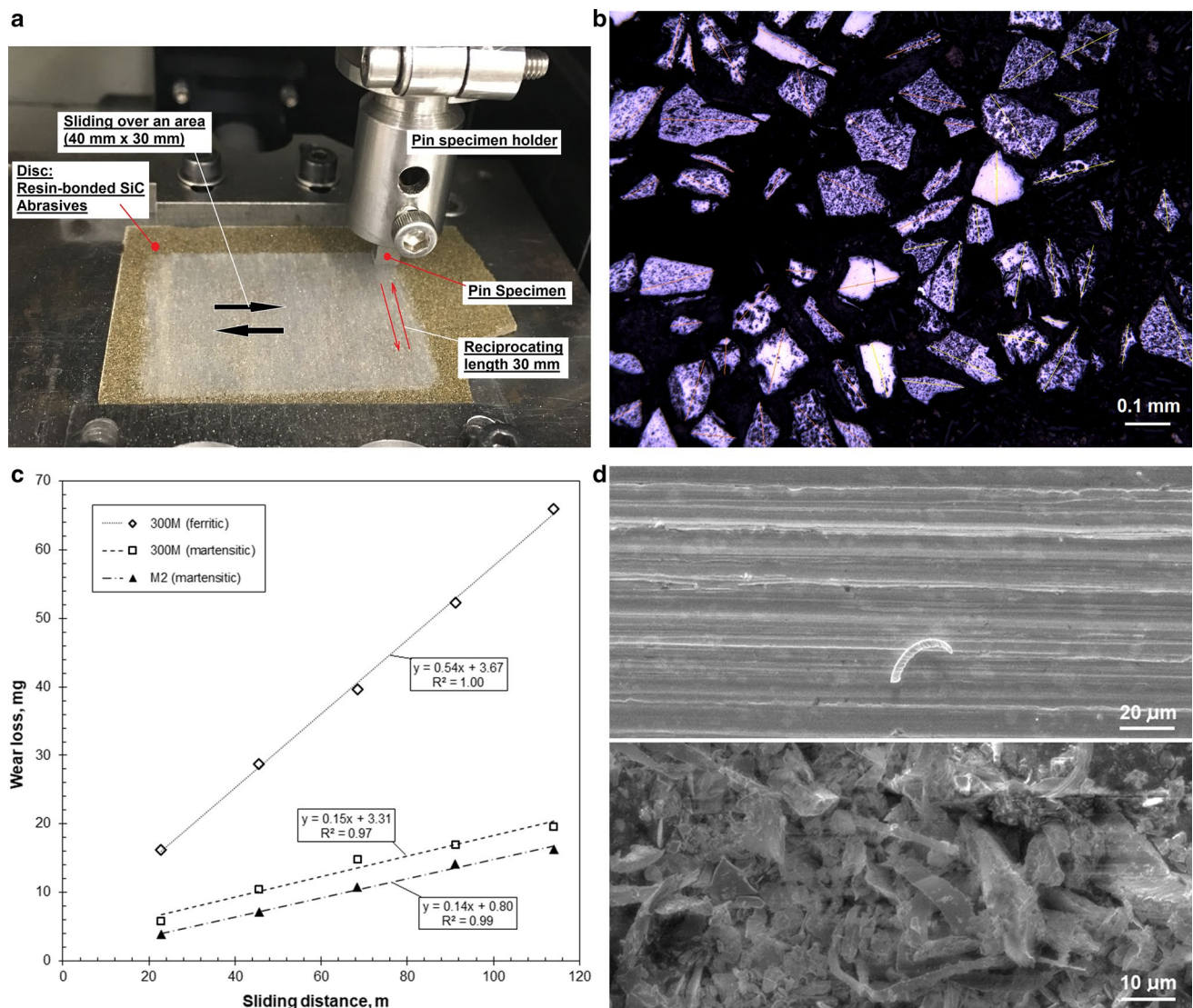
Fig. 2 Configuration of the two-body abrasive test: **a** the reciprocating abrasive wear test; and **b** morphology of the SiC abrasive in a polished section; **c** mass loss plotted versus sliding distance of three ferritic and martensitic steels; and **d** morphology of resultant worn surface

expressed as volume loss at unit applied load and unit sliding distance, i.e., $m^3 \, N^{-1} \, m^{-1}$. In the testing, the frictional load was simultaneously monitored and acquired to the computer to determine the friction property.

Since this abrasive test was designed and conducted in the first time, repeated tests were carried out using a ferritic steel (annealed 300 M, HV 3.4 GPa) and two martensitic steels (300 M, HV 7.2 GPa, and high-speed steel BM2, HV 8.6 GPa), in order to verify the reproductivity. Figure 2c shows some results of the verifying tests, in which the mass losses exhibit good linear relationships to the sliding distance. Figure 2d shows typical views of the worn surface and wear debris. The worn surface shows straight parallel ploughing grooves. The wear debris particles were from a used abrasive disc, comprising long debris, fine wear debris, and broken

SiC abrasives. The long debris shows naturally curved shape produced by micro-cutting mechanism. The broken SiC abrasives mostly have sharp edges. These features confirm micro-cutting as the predominant wear mechanism.

The microstructure of the heat treated samples was characterised using optical microscopy (OPM) and scanning electron microscopy (SEM). All the metallographically polished samples were etched using 2% nital prior to observation. A FEI Nova200 FEG-SEM was employed to observe the microstructure and wear products, including worn surfaces and collected wear debris. In addition, cross-sectional samples were prepared after the wear tests to examine wear induced microstructure changes beneath the worn surfaces. Cross-sectional specimens were prepared for transmission electron microscopy (TEM) following the longitudinal

(sliding) direction of the worn samples. The methodology of cross-sectional worn sample analyses can be found in a recent publication [30]. TEM observation was undertaken on a field-emission transmission electron microscopy JEOL 3100F operating under 200 kV.

X-ray diffraction (XRD) analyses were carried out using an Empyrean X-ray diffractometry (PANalytical B.V., Netherlands) with cobalt radiation (K_α-Co, $\lambda = 0.1789$ nm). Five diffraction peaks were acquired at a step size 0.026° and a nominal step time 1,000 s, including the (200), (220) and (311) peaks of austenite and the (200) and (211) peaks of bainitic/martensitic (B/M) ferrite. Several quantitative analyses were performed on the obtained diffraction peaks. Firstly, the peak positions (2θ), integrated intensities (I), and peak broadening width (β), i.e. the full-width-at-half-maximum (FWHM), were measured on the five diffraction peaks using a self-developed Gaussian multiple peak fitting process [28, 31]. These measurements were employed to calculate volume fraction of retained austenite using the direct comparison method recommended in literature [32]. The micro strains (ε) of the austenite and B/M ferrite were estimated using the Scherrer equation $\varepsilon = \frac{0.25 \cdot \beta \cdot \cos\theta}{\sin}$ [33], respectively. Then the d-spacings calculated from the three austenite diffraction peaks (200), (220) and (311) were used to estimate the lattice parameter a_0 and thereafter the carbon content C_γ (in weight percentage wt%) of austenite. For the latter, a linear relationship between a_0 and C_γ has been expression as $C_\gamma = \frac{a_0 - 0.3555}{0.0044}$ [28].

3 Results

3.1 Microstructure Evolution with Increasing Austempering Time

Although OPM has inferior spatial resolution in observing fine microstructure of the steel, OPM observations revealed initial formation of bainitic ferrite and its subsequent growth with increasing austempering time. Selected results are presented in Fig. 3. In Fig. 3a, the microstructure of the sample WQ show typical acicular martensite morphology. The areas of lath-shape martensite (labelled 'M-lath' in Fig. 3a) exhibited preferential etching over the areas of plate-shape martensite (labelled 'M-plate' in Fig. 3a). Such heterogeneous microstructure distributions
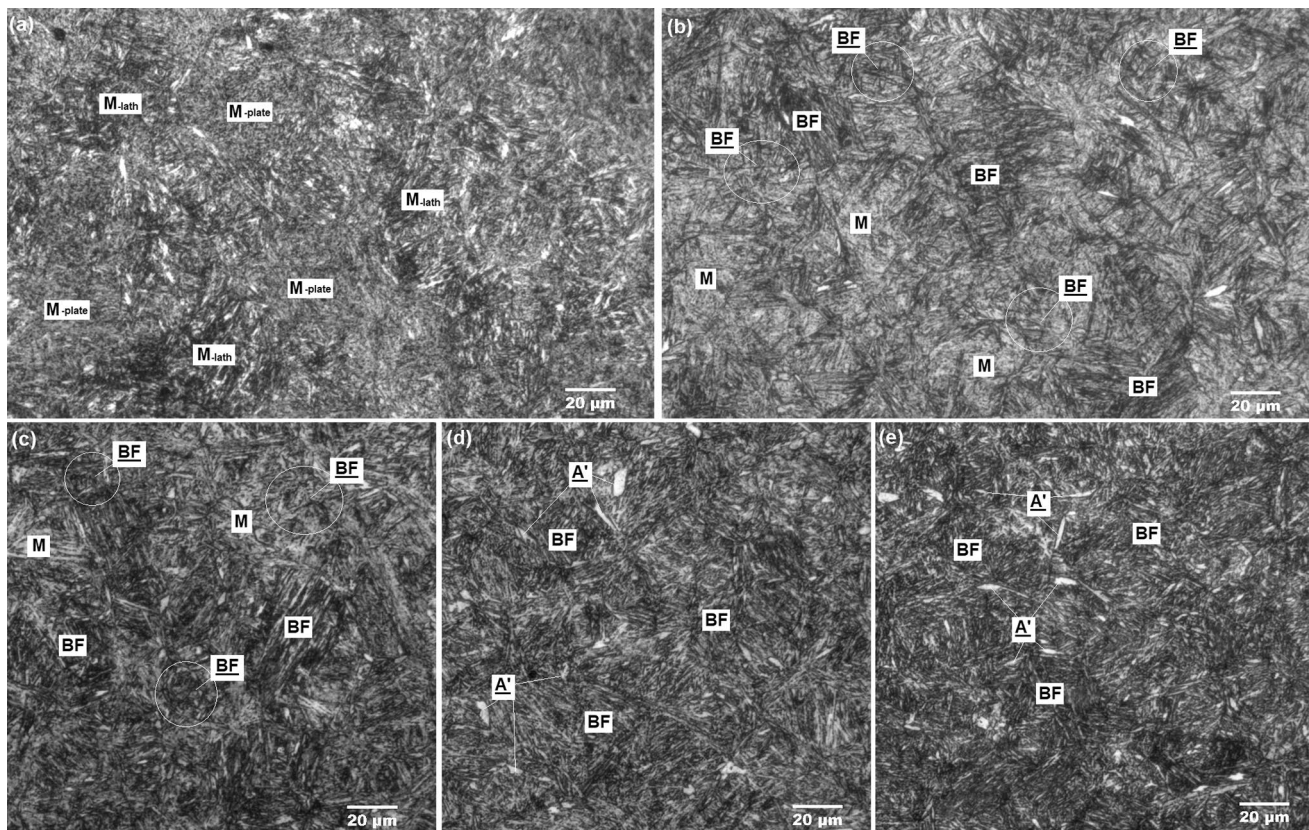

Fig. 3 Optical microscopic images showing microstructure evolution with increasing austempering time t: **a** t = 0 min (WQ); **b** t = 10 min (T-10); **c** t = 20 min (T-20); **d** t = 30 min (T-30); and **e** t = 60 min (T-60)

were attributed to the dendritic segregation during steel casting. The sample T-10 exhibited strong preferential etching by showing large quantity of black-contrast needles, Fig. 3b. These needle-shape grains are known to be bainitic ferrite (labelled as 'BF' in the image) as compared to the light-contrast martensite (labelled 'M' in the image). In addition, careful observation of optical images revealed that, some areas show high density of BF needles where the needles are parallel to each other, whereas the rest areas show individual BF needles having angular distribution, seeing Fig. 3b. These features indicate the formation and initial growth of bainite. Kang reported an incubation period prior to bainite transformation [3, 8]. Our research suggests that the incubation period of the 300 M steel at the applied austempering temperature is less than 10 min.

Figure 3c is the OPM microstructure of the sample T-20, in which bainite is the predominant microstructure constituent as compared to the small, insulated areas of martensite. Figures 3d, e show similar homogeneous presence of bainite, which reveals that bainite transformation took place across the whole volume although further bainite growth could still be time dependent.

Figure 4 is a collection of SEM images providing a detailed comparison between the martensite of the water-quenched sample and the initial bainite of the 10-min austempered sample. The low-magnification image of the martensite in Fig. 4a corresponds to the heterogeneous distribution of martensitic laths and plates in Fig. 3a, in which the areas marked 'I' and 'II' refer to the dark- and bright-contrasted areas respectively. Area 'I' shows straight martensitic laths parallel to each, Fig. 4b, whereas area 'II' shows less-etched martensite plates with random orientations, Fig. 4c. In Fig. 4d, the low-magnification SEM image shows large quantity of BF needles of the sample T-10, which is consistent to the OPM image (Fig. 3b). The straight, narrow BF needles distribute non-homogeneously in the microstructure that some are parallel arrays co-existing with filmy austenite, whereas other BF needles having irregular orientations have partitioned the matrix as large number of small and narrow areas to each other, Fig. 4e. In Fig. 4f, the
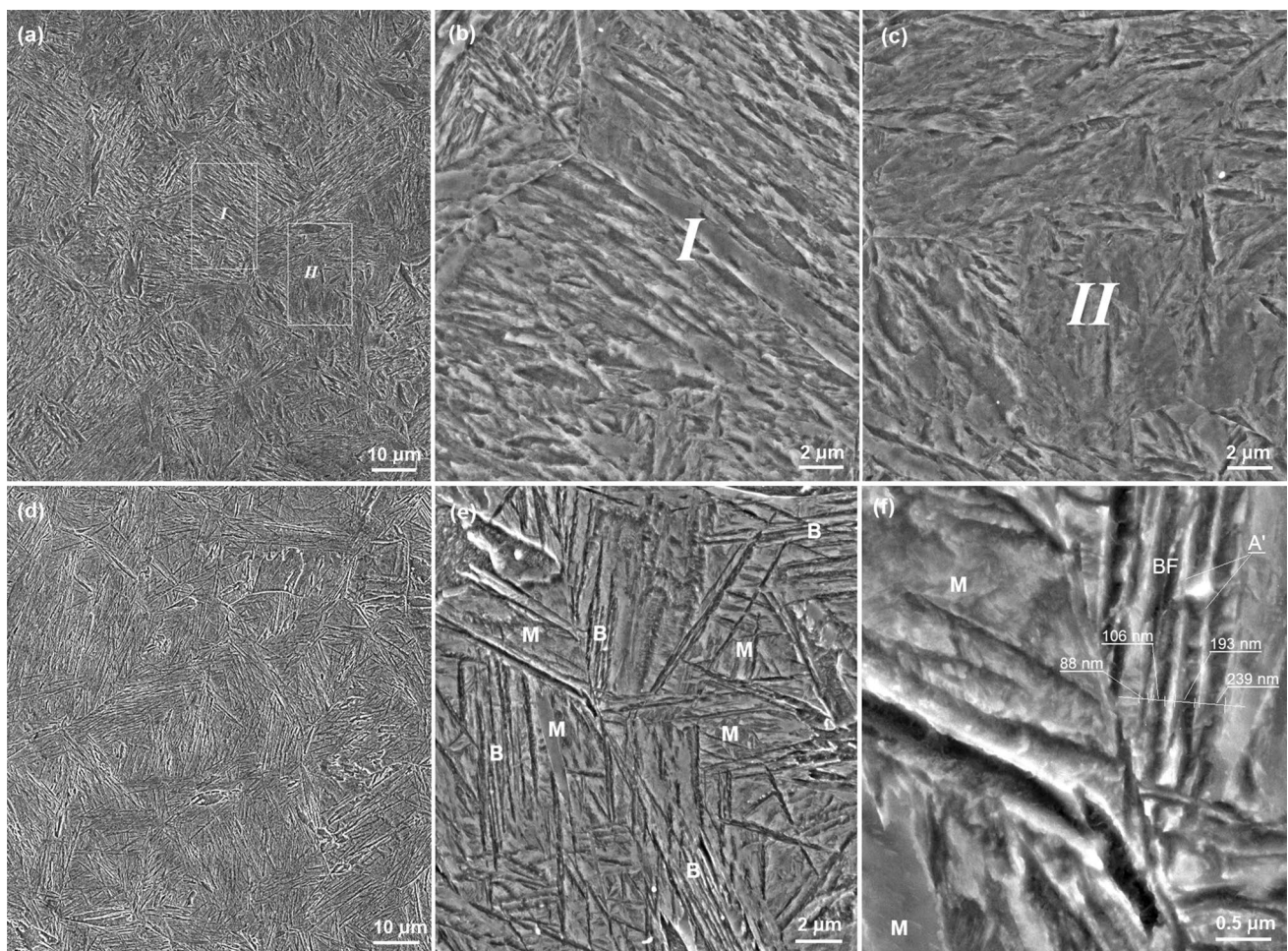

Fig. 4 SEM images to compare the microstructure of **a–c** sample WQ and **d–f** sample T-10

initial BF needles are measured in sub-micro to nano width (80–170 nm), whereas the inter-lath austenite films show an average thickness of approximately 50 nm.

Figure 5 shows SEM observations of the austempered samples T-30 and T-60. Both samples exhibit similar microstructures. In the low-magnification images, Fig. 5a, d, the distributions of BF needles become homogeneous, indicating completion of the bainite transformation. In Fig. 5b, e, the bainite matrix comprises parallel BF arrays and nano-width filmy austenite. In the areas where the BF needles exhibit angular distribution, blocky austenite grains have been resulted. The high-magnification images (Fig. 5c, f) show details of the filmy austenite, blocky austenite and the BF matrix. The fine bright features in some thick BF plates are carbide precipitates, which has been verified by observing a sample being etched with Kailings' No. 2, seeing the inserted image in Fig. 5f. The observation also confirmed that most thin BF needles are free from carbide precipitates. The carbide precipitation implies further decarbonisation of the BF matrix, which was attributed to the lower Si content of the sample steel than those Si-Mn-Cr alloyed steels having carbide-free BF and austenite microstructure [10–12]. Nevertheless, the microstructure characterisation has confirmed the completion of bainite transformation when the austempering time was 30 min, whereas further extended austempering did not bring about significant evolution of the microstructure.

3.2 Quantitative X-ray Diffraction Analysis

Figure 6 is the XRD patterns of the austempered and quenched samples, in which the austenite diffraction peaks show two changes with increasing austempering time. The first change is the increased peak height with increasing austempering time, which indicates promoted austenite retaining. The second change is the asymmetric shape of the austenite peaks, as marked by arrows. The asymmetric shape implies the appearance of two overlapping peaks having certainly different peak positions. Considering the filmy and blocky austenite constituents as observed by SEM, Fig. 5, the asymmetric austenite peaks confirm different lattice parameters and carbon contents of the filmy and blocky
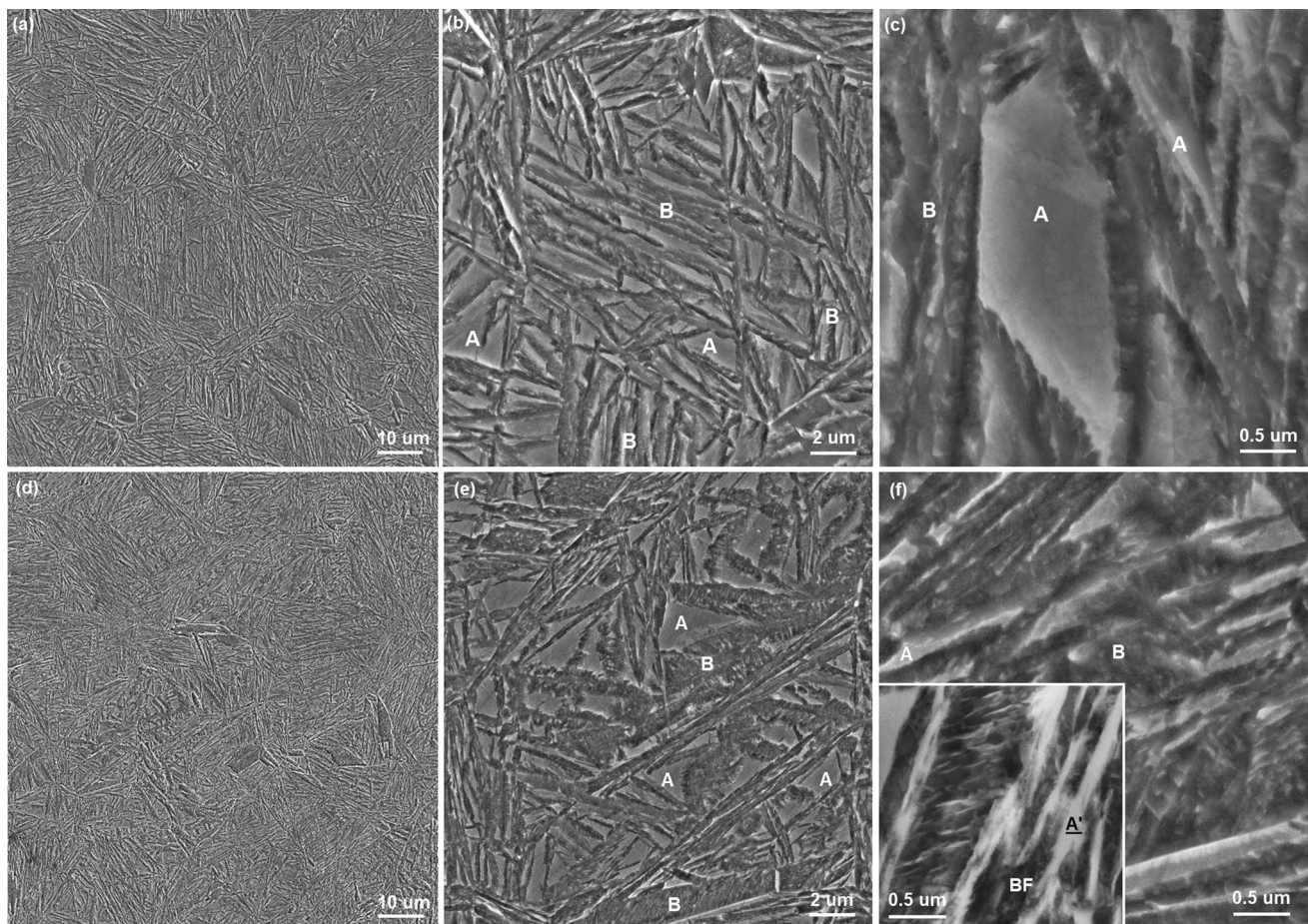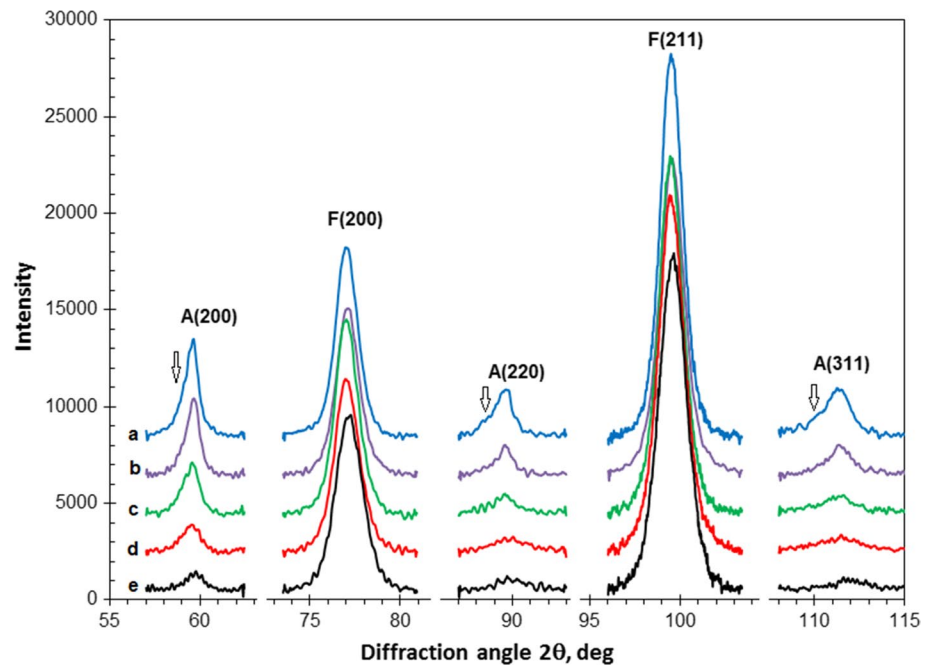

Fig. 5 SEM images showing the microstructure of **a–c** sample T-30 and **d–f** sample T-60

Fig. 6 The XRD peaks of the heat treated samples **a** T60; **b** T-30; **c** T-20; **d** T-10; and **e** WQ


austenite. Such phenomenon has been reported by other researchers [3, 4, 14].

Figure 7 illustrates the variation of austenite volume fraction and carbon content with increasing austempering time. The volume fraction exhibits an approximately linear relation to the austempering time. Meanwhile, the austenite exhibits a linear increase in the carbon content in the short-term austempering up to 20 min, i.e., from 0.83 to 1.16%, while further austempering did not enrich the carbon concentration.

Considering the asymmetric shape of the austenite peaks acquired on the 60 min austempered sample, Fig. 6, multiple Gaussian peak fitting has been applied to retrieve the overlapping filmy and blocky austenite

Fig. 7 Volume fraction and carbon content of retained austenite plotted versus austempering time
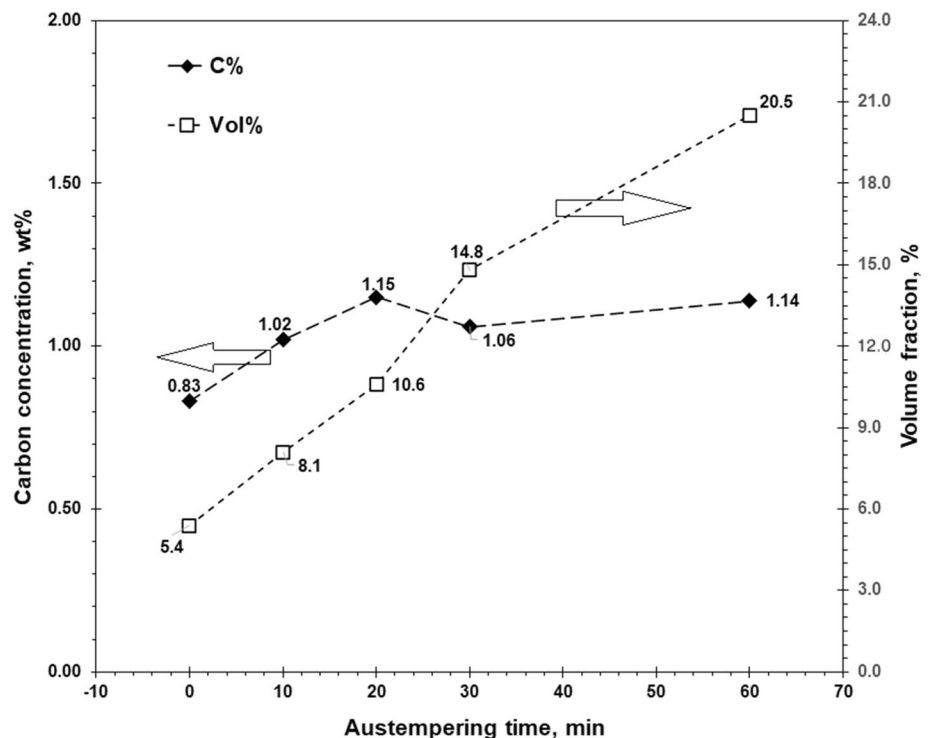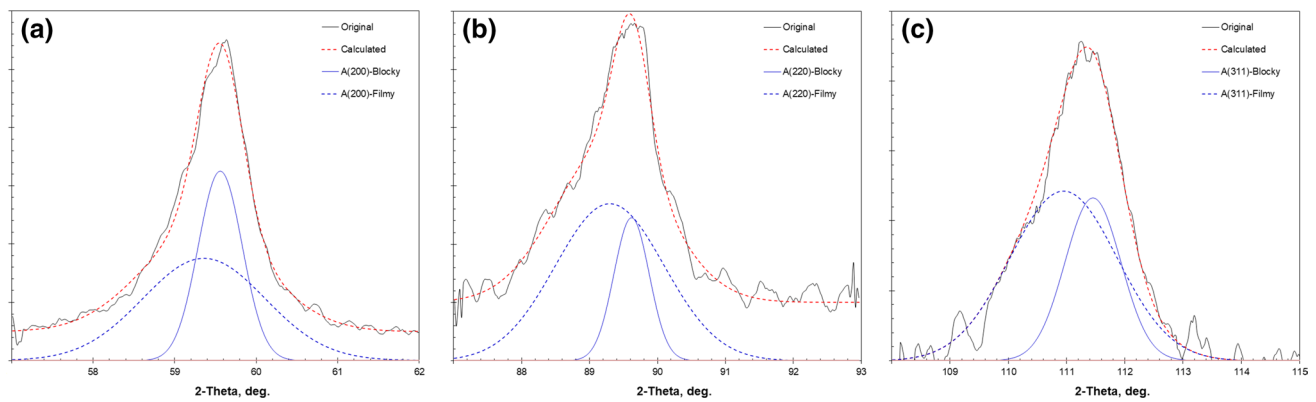
Fig. 8 Gaussian peak fittings of the austenite diffractions of the austempered sample T-60: **a** A(200); **b** A(220); and **c** A(311)

Table 1 Properties of filmy and blocky retained austenite quantified by Gaussian peak-fitting

	Vol%	Lattice a_0, nm	C %	Strain, %
Filmy austenite	13.7	0.3605 ± 0.0007	1.29 ± 0.16	0.94 ± 0.11
Blocky austenite	6.8	0.3594 ± 0.0007	1.04 ± 0.16	0.37 ± 0.11

peaks. The results are provided in Fig. 8 for the A(200), A(220) and A(311) peaks, whereas the quantification is summarised in Table 1. Combining the SEM observation and the XRD analysis, the volume fractions of filmy and blocky austenite in the austempered sample T-60 accounts for 13.7% and 6.8%, respectively, whereas the former has higher carbon content (1.29%) than the latter (1.04%).

The micro strains of the ferritic and austenitic phases were estimated from the FWHM measurements of the M(200)&(211) and A(200) peaks respectively. With increasing austempering time, both the B/M ferrite and the retained austenite show lower lattice strains respectively, Fig. 9. The hardness property is also plotted, which matches well to the variation of the micro strains and the increase of retained austenite fraction.

Fig. 9 Correlation between the hardness and micro strains with increasing austempering time
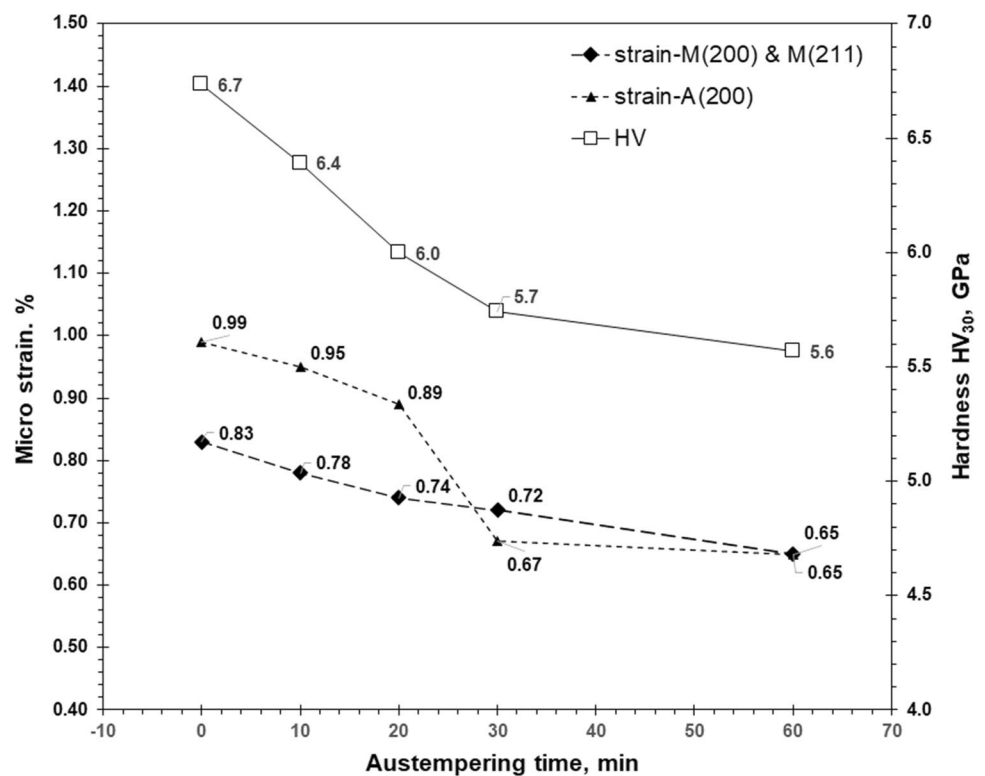
3.3 The Abrasive Wear Property

The wear properties of the tested samples are illustrated in Fig. 10. In Fig. 10a, the mass losses are plotted versus sliding
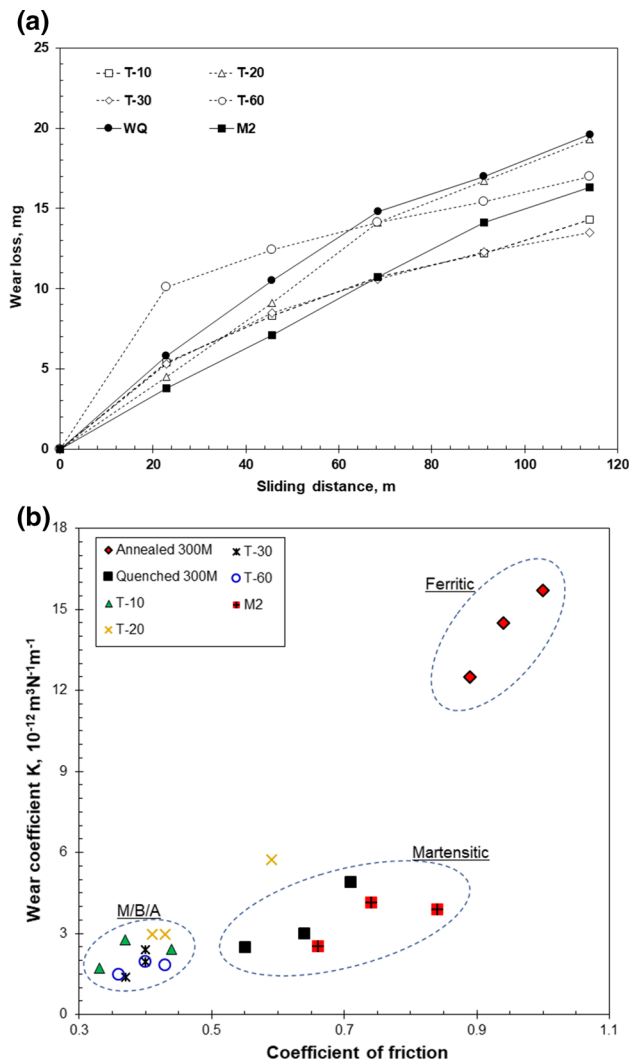

(a)

(b)

Fig. 10 Wear property of the tested samples: **a** Mass loss plotted versus sliding distance; and **b** Correlation between the wear coefficient and average friction coefficient

distance. The two martensitic samples (M2 and WQ) exhibit nearly linear increase of mass loss with sliding distance. In contrast, most of the austempered samples (T-10, T-30 and T-60) show slightly fast wear in the beginning before stabilising a linear relationship. Considering that the first two measurements in each test were affected by a running-in period and the formation of conformal contacting between the pin and the abrasive disc, the last three measurements were employed to calculate the wear coefficient values.

The wear coefficients and friction coefficients are summarised in Table 2 and illustrated in Fig. 10b where the wear coefficients are plotted versus the related friction coefficients. The properties can be classified into three groups. All the austempered samples show low coefficients of wear and friction, having average values of 2.47×10^{-12} $m^3 N^{-1} m^{-1}$ and 0.47, respectively. In contrast, the martensitic steels show slightly higher wear coefficients and substantially higher friction coefficient than the austempered samples, in values of 3.48×10^{-12} $m^3 N^{-1} m^{-1}$ and 0.67, respectively. The annealed 300 M steel is the third group which shows both the highest coefficients of wear and friction. In the austempered samples, longer austempering times of 30 and 60 min seem to lead to the lowest wear coefficient. Moreover, it is also noticed that even a short austempering of 10 min brought about a remarkable decrease in the wear coefficient from 3.5 to 2.3×10^{-12} $m^3 N^{-1} m^{-1}$.

Table 2 and Fig. 10b reveal that, the different wear property is correlated to the friction behaviour. Obviously, the annealed steel shows the largest coefficient of friction followed by the quenched steel. The austempered samples show substantially lower friction than the annealed and quenched sample. The different friction behaviour suggests different response of microstructure to the applied abrasive load.

3.4 SEM, TEM and XRD Analyses of Wear Mechanisms

Figure 11 shows selected SEM images of the worn surfaces. In Fig. 11a, the worn surface of sample WQ (martensitic 300 M) is full of straight ploughing grooves. A long curved wear debris remains connection to the worn
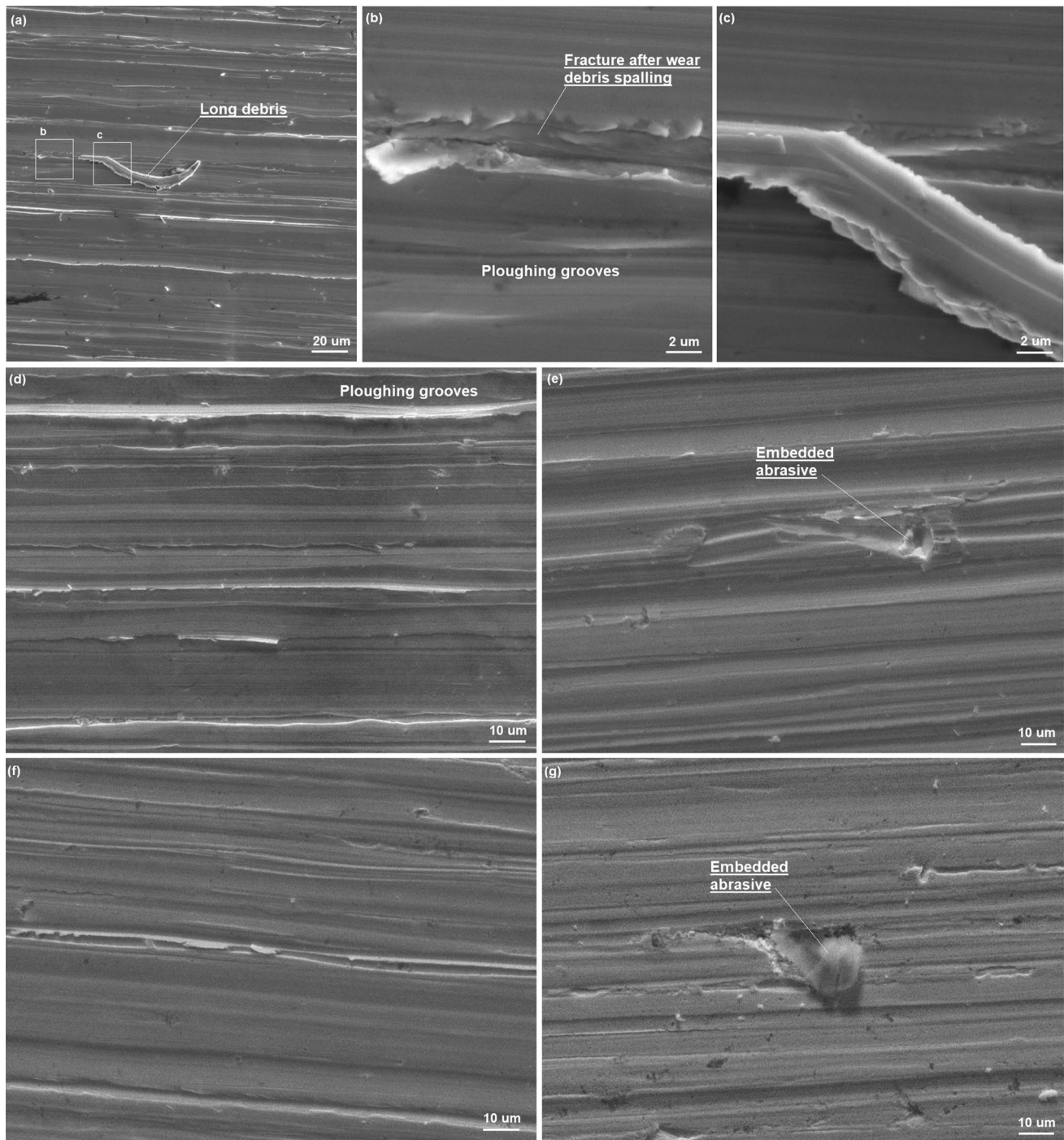
Table 2 The sliding abrasive wear properties of all the tested samples

Sample	Wear coeff., 10^{-12} $m^3 N^{-1}$ m^{-1}				Friction coeff			
	Test 1	Test 2	Test 3	Mean	Test 1	Test 2	Test 3	Mean
T-10	2.8	1.7	2.4	2.3	0.71	0.55	0.64	0.63
T-20	3.0	3.0	5.7	3.9	0.41	0.43	0.59	0.48
T-30	2.4	2.0	1.4	1.9	0.40	0.40	0.37	0.39
T-60	2.0	1.5	1.8	1.8	0.40	0.36	0.43	0.40
Annealed 300 M	12.5	14.5	15.7	14.2	0.89	0.94	1.00	0.94
WQ	4.9	2.5	3.0	3.5	0.71	0.55	0.64	0.63
Martensitic BM2	4.1	3.9	2.5	3.5	0.84	0.66	0.64	0.71

Fig. 11 SEM images showing abrasive wear features of selected samples: **a–c** WQ; **d** T-10; **e** T-20; **f** T-30; and **g** T-60

surface, where the two highlighted areas are shown in Fig. 11b, c, respectively. In Fig. 11b, the rough band between two ploughing grooves shows features of local fracture after a long wear debris detached from the parent surface. Note that the fracture exhibits little evidence of shear deformation, which implies localised embrittlement as a sequence of strain hardening. The strain hardening

has been confirmed by comparative micro-hardness measurements, to be shown in next section. Figure 11c shows the area where the wear debris was under progressive detaching from the worn surface. Similar ploughing features were also observed on the worn surfaces of other samples, Figs. 11 d–g, which confirm both micro-cutting mechanism, seeing the wear debris chips in Fig. 2d, and

ploughing deformation. In particular, the edges of ploughing grooves were also subjected to wear debris formation as a result of repeated deformation and strain hardening.

The ploughing deformation can be observed in more details in the cross-sectional SEM and TEM. Figure 12 is a longitudinal vertical section of the T-30 worn surface, showing wear induced shear deformation behaviour of the M/B/A microstructure. In SEM observation, the cross-section specimen was tilted by 10° in order to observe both the worn surface (the bright rough top part) and the metallographically etched subsurface microstructure simultaneously. Shear deformation can be seen in depths up to 2.5 μm. To observe more details of the shear deformation, the two regions (marked 'I' and 'II') are presented in a higher magnification. On the top worn surface in depths less than 1.5 μm, the microstructure become disordered as a results of the severe deformation. Beneath the disordered top layer is the bainitic ferrite (deep-etching) and filmy austenite (light-etching) structures showing conformal bending deformation. Despite the severe deformation, no crack was observed either in the top layer or in the subsurface, revealing the role of good plasticity of the austenite in the shear deformation.

Considering the small depths of deformation as observed in the vertical cross-sections, a cross-section was prepared at a small and inclined angle of approximately 5°, Fig. 13. Several ploughing grooves locate in the left hand side of Fig. 13a. Note that the applied 2% natal-etching resulted in different microstructural view of the grooves as compared to the nearby microstructure. The extremely fine features could only be observed at very high magnification, e.g., Fig. 13b. Such fine features refer to the sliding induced refinement. In addition, bending deformation of the BF laths can be seen in close vicinity of the ploughing grooves, Fig. 13a. One deformed area is highlighted in Fig. 13b at higher magnification. Moreover, nanoscale parallel lines in some austenite blocks indicate twinning deformation, seeing the 'X'-marked points in Fig. 13b.

Figure 14 shows typical results of cross-sectional TEM observations of the worn samples. Figure 14a is a low-magnification image showing the whole thickness of plastically deformed worn surface. The region labelled 'I' is the ion-beam milling induced deposit of re-sputtered species (mainly from the copper grid and the steel sample) providing a precise guide of the top worn surface. The abrasive wear resulted in a layered structure of the worn surface

Fig. 12 A longitudinal cross-sectional SEM of worn surface showing wear induced surface deformation
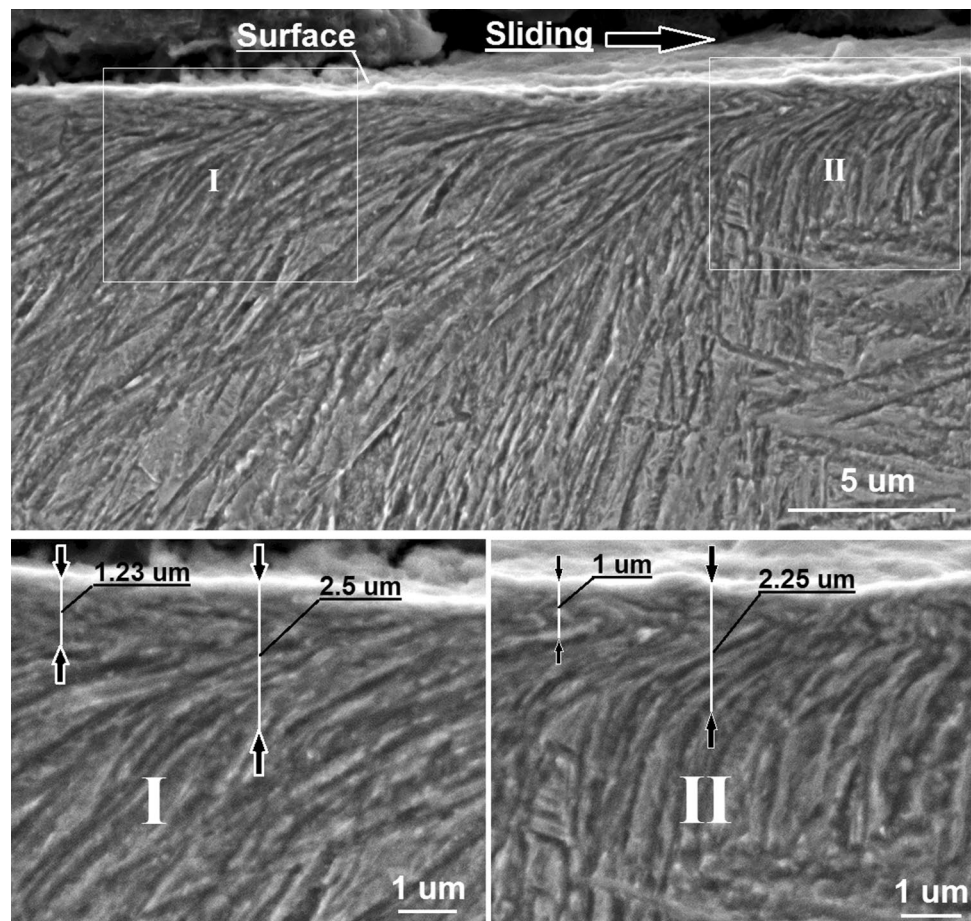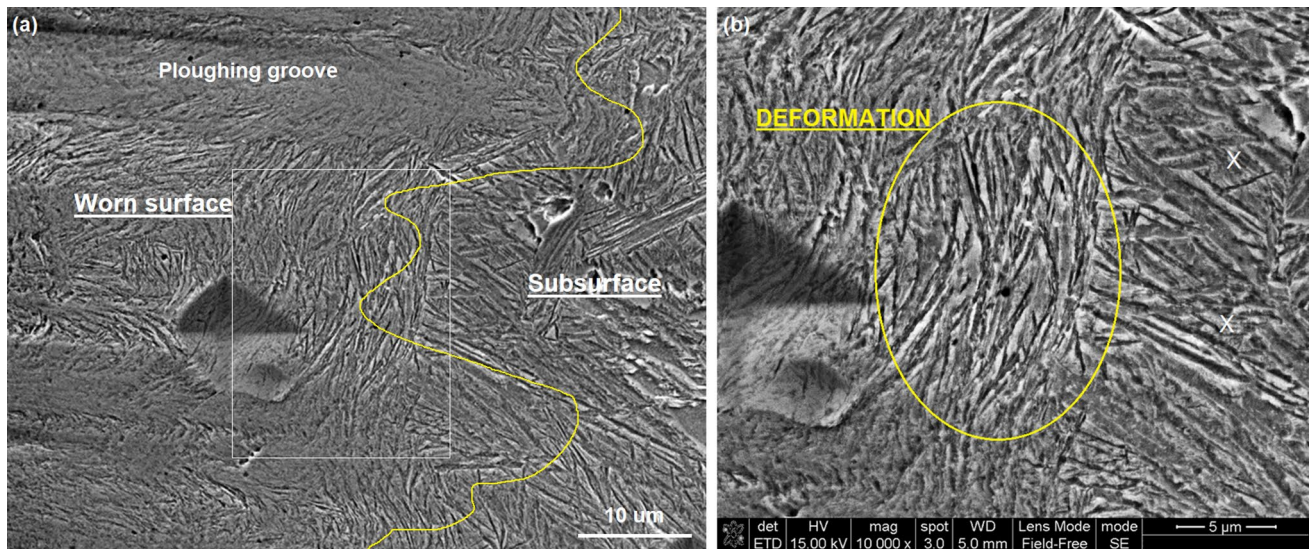
Fig. 13 SEM images of a 5°-inclined cross-section of the worn surface of austempered 300 M sample T-30 to show wear induced deformation in the bainitic ferrite

Fig. 14 Longitudinal cross-sectional TEM of a worn surface: **a** the layered structure of the deformed worn surface; **b** a selected electron diffraction pattern of the deformed layer; and **c** high-magnification view of the top nanolaminate layer
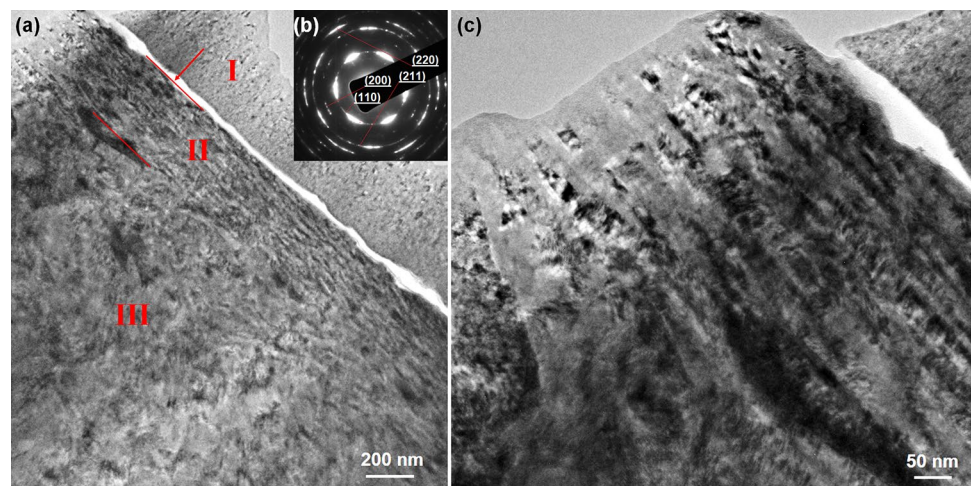
comprising a nano-laminated top layer (labelled 'II') and a subsequent layer of shear deformation (labelled 'III') before reaching the un-deformed bulk material. The nano-laminate top layer is shown in more details in Fig. 14c, which confirms the occurrence of extremely severe plastic deformation. The depth of the laminate layer is about 400–450 nm, having laminating thickness of 20–30 nm. Figure 14b is a selected area electron diffraction pattern acquired in the deformed laminate region, in which the arc-like patterns suggest the polycrystalline nature. These patterns refer to the lattice planes of (110), (200), (211) and (220) of the bainitic/martensitic ferrite. However, the TEM analysis was not able to preclude the presence of retained austenite because of overlapping between the

ferrite patterns and possible austenite patterns, such as F(110) (d = 0.2027 nm) and A(111) (d = 0.2080 nm).

In order to clarify the presence of any austenite in the wear induced deformation layer, comparative studies were made by acquiring XRD patterns from both the bulk steel and the worn surface, in which the obtained diffraction patterns were analysed using a multiple Gaussian peak-fitting method as described earlier. The results are presented in Figs. 15a, b. The bulk steel (sample T-60) shows a distinct low-intensity diffraction peak left to the main F(110). Peak retrieving analysis reveals the presence of filmy and blocky austenite in both the bulk steel (Fig. 15a) and the worn surface (Fig. 15b), which is consistent to the results as described in Fig. 8. Comparing to the bulk steel, the
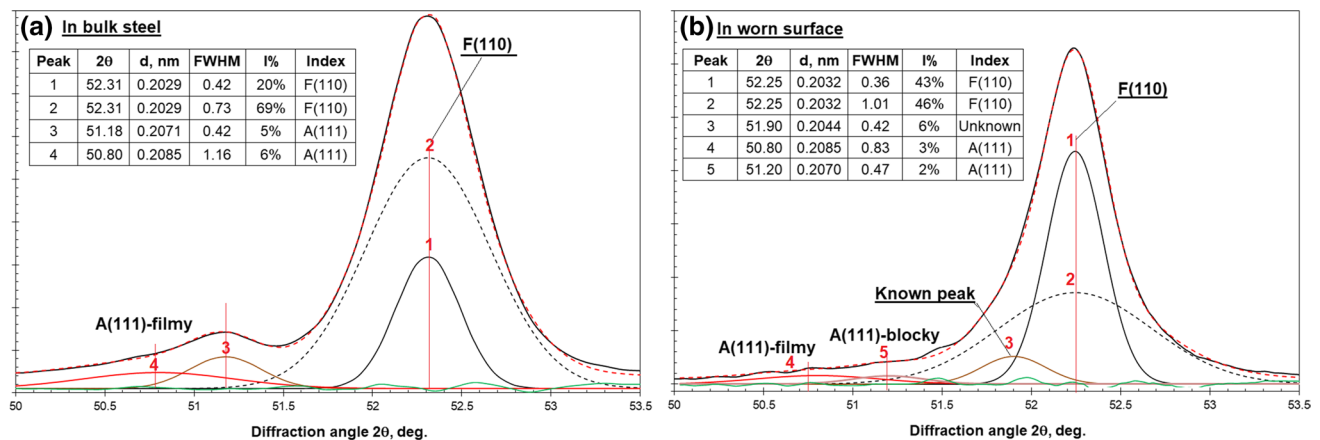
Fig. 15 Comparative XRD analysis of retained austenite **a** prior to and **b** after the abrasive wear. Note the absence of A(111)-blocky peak in the worn surface

worn surface shows remarkable decrease in the integrated intensity of the filmy and blocky austenite peaks, namely, from 6 to 3% of the former and from 5 to 2% of the latter respectively. The comparative XRD analysis suggests partial transformation of retained austenite as a sequence of wear induced deformation.

In addition, the F(110) peaks each fit to two Gaussian profiles, which can be interpreted as two types of martensitic and bainitic ferrites having the same lattice parameter but different micro-strains. Obviously, this phenomenon attracts interests of further comprehensive study. Nevertheless, the quantitative XRD reveals that, the applied sliding abrasive wear resulted in a change in the ratio of the two ferritic sub-peaks. The variation implies wear induced evolution of the sub-structures, i.e., increased amount of low-strain martensitic/bainitic ferrite.

### 3.5 Strain Hardening Caused by the Abrasive Wear

Considering wear induced plastic deformation, the related strain hardening behaviour was evaluated by measuring the Knoop hardness properties of the worn surfaces as compared to the bulk samples. The results are shown in Fig. 16a. All the worn surfaces show substantial hardening as compared to the bulk. The austempered samples show straining hardening, between 1.4 and 2.2 GPa, which is comparable to the strain hardening of the martensitic steels (2.0–3.0 GPa) and is more pronounced than the ferritic sample (1.4 GPa). Micro-hardness measurements were also made on the inclined worn surface cross-section (Fig. 12). The results are plotted in Fig. 16b to show a hardness profile in depths up to 50 μm, in which a hardened layer of about 5–10 μm has been detected.

4 Discussion

4.1 The Microstructure Evolution in the Low-Temperature Austempering

We found that the applied short-term austempering treatments led to multi-constituent microstructure including fine BF laths, martensite and increased retained austenite, Figs. 3 and 4. The isothermal holding, even at the low temperature close to the Ms point, promoted nucleation of bainitic ferrite at the grain boundaries of undercooled austenite. The phase transformation of the austenised steel in the short-term austempering can be understood to happen in such a sequence that nucleation of bainitic ferrite took place in the grain boundary areas of undercooled austenite. In literature, these areas were characterised to be depletion in carbon [3, 8]. Then the initial bainitic ferrite grew as parallel needle-like grains accompanied by carbon partitioning between the BF needles and the adjacent austenite, whereas the carbon partitioning resulted in carbon-enrichment in the austenite and carbon-depletion in the BF grains. In this period, fine carbide may precipitate coherently in the BF grains for the low silicon content of the steel was not enough to prohibit its occurrence. The BF growth stopped when the austempering process was terminated. Subsequently, the rest austenite transformed to martensite with retained austenite when the steel was cooled continuously to room temperature. Comparing to the conventional austenite to lower bainite transformation, the lower transformation temperature greatly restricted the kinetic growth of the BF laths, resulting in their extremely small widths. The BF laths intersected the austenite grains and led to refined martensite grains in the subsequent

Fig. 16 **a** Micro hardness measured both on the worn surfaces and on the bulk materials. The values labelled inside the columns are hardness increments induced on the worn surfaces. **b** Micro hardness depth-profile beneath the worn surface of austempered sample T-30

(a)

(b)
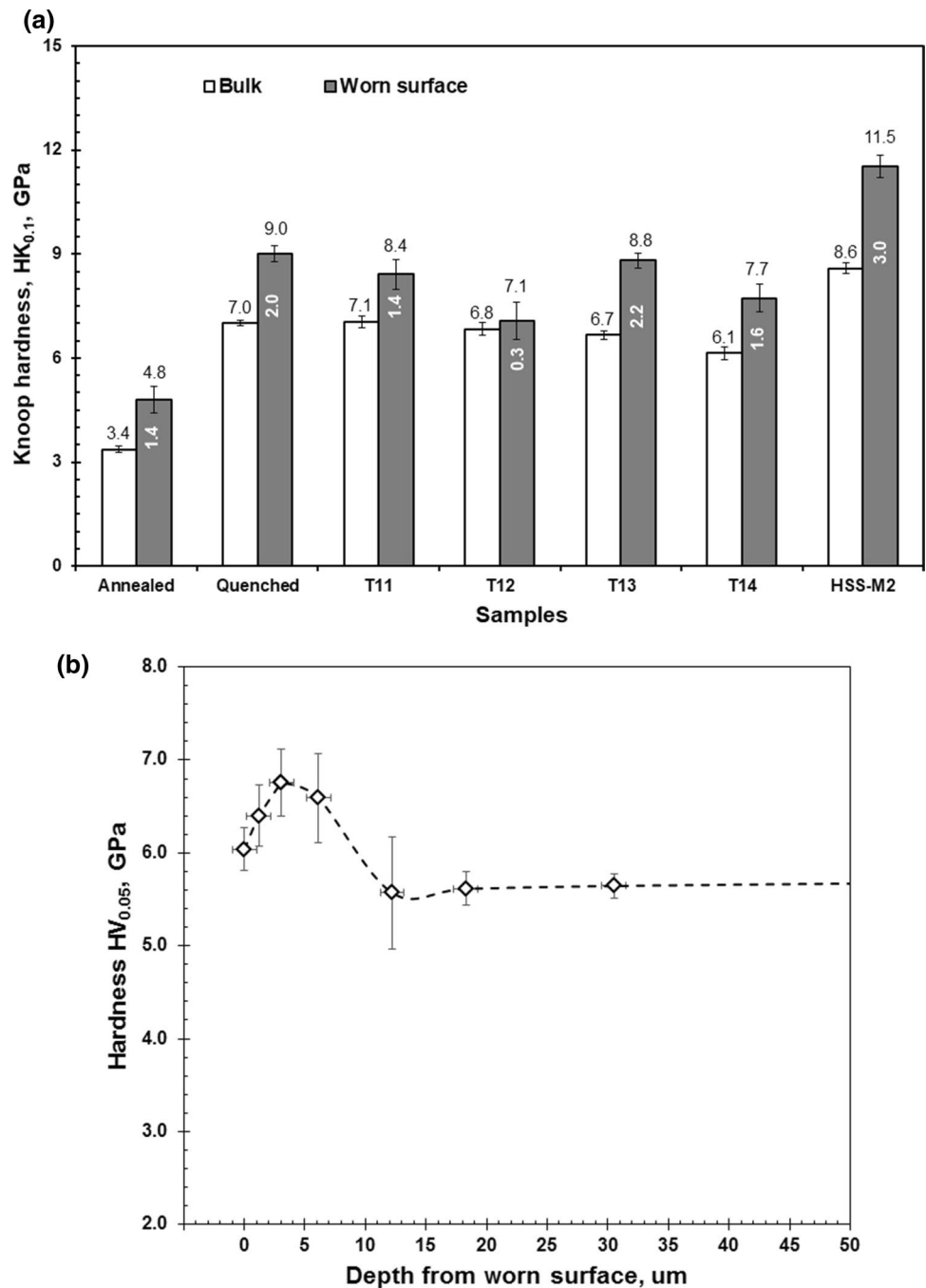
cooling. This phenomenon supports the strengthening mechanisms proposed by Tomita [7].

We also found correlation between the variation of hardness with increasing austempering time. It is interesting to note that high hardness, comparable to the hardness of as-quenched martensite, has been maintained when the austempering time was not exceeding 20 min. The high hardness would help reserve its good wear resistance.

The initial BF growth facilitated carbon partitioning between the newly formed BF and the nearby austenite.

This finding is consistent to literature [4, 12, 28]. Such phenomenon was more pronounced in the first 20 min of the transformation, in which both the carbon concentration and volume fraction of retained austenite increased with austempering time.

In addition, the coarsening of BF and considerable amount of blocky austenite were resulted from the extended isothermal time of 30–60 min. Quantitative XRD has revealed different carbon contents of the filmy and blocky austenite, Table 1.

4.2 Effect of Microstructure on the Two-Body Abrasive Wear Property

The two-body abrasive wear testing employed in this research represents a common wear mode of metallic alloys caused by hard and angular abrasives. Under this defined wear condition, the austempered steel exhibited superior wear resistance. Therefore, austempering treatment can be considered as a good alternative to the conventional Q–T hardening process.

Three types of microstructure have been evaluated in current wear tests, namely bainitic/martensitic/austenitic structure of the austempered 300 M, martensitic structure of the water-quenched 300 M and the hardened M2 steel, and ferritic structure of the annealed 300 M steel.

The martensitic steels exhibited excellent wear resistance owing to the highly hardened microstructure as compared to the ferritic steel. In contrast, the ferritic structure has experienced high friction coefficient and high wear rate with a coefficient in the scale of 10^{-11} m^3 N^{-1} m^{-1}. It is known that the high hardness of martensite is able to greatly restrict the indenting deformation, micro-cutting and ploughing deformation arising from the hard abrasives. In current experiments, higher hardness of the quenched and austempered samples greatly restricted the depth of worn surface deformation, resulting in significantly reduced wear and friction coefficients. Comparing the wear coefficients of the ferritic steel with others, hardness is certainly an essential property of wear resistant materials, as low hardness triggers deeper penetration of abrasive particles which consequently make more effective micro-cutting in addition to the more pronounced deformation. Such ploughing deformation as part of the applied abrasive wear has been confirmed by cross-sectional SEM and TEM observations, Figs. 12, 13, and 14.

The superior wear resistance of the austempered samples has confirmed the beneficial role of multiphase microstructure in resisting abrasive wear. In particular, carbon partitioning during the austempering process led to preferential carbon enrichment in austenite and depletion in BF laths, whereas both facilitated plastic straining in the sliding wear. As observed in cross-sectional TEM and SEM, the occurrence of severe shear deformation should have been attributed to this superior plasticity of the retained austenite. As a result, its wear coefficient become remarkably lower than the martensitic steels even though the latter have higher hardness. This is in good consistent to the role of austenite in similar abrasive processes reported by other researchers [15, 17, 18, 20, 21, 24, 26].

The contribution of retained austenite to the lower wear coefficient can be understood by the following aspects.

Firstly, the austenite-containing samples also recorded lower friction than the martensitic samples. Cross-sectional SEM and TEM of the worn samples have observed conformal shear deformation in the subsurface microstructure of bainitic ferrite laths and the inter-lath filmy austenite, Fig. 12. Obviously, the austenite phase reduced the resistance of the shear deformation owing to its good plasticity, whereas good local plasticity was able to release the concentrated stresses in front of the micro-cutting zones. As a result, it favourited more ploughing deformation instead of direct mass removal by micro-cutting in martensite-dominated structure [19].

Secondly, the current experiment results do not support a conclusion that it was the straining-induced work hardening and martensite transformation which resulted in the superior wear resistance of the austempered samples. In literature, wear induced transformation of retained austenite to martensite were repeatedly claimed [16–18, 20, 23, 34–36]. Although most of their experiments found the decrease of retained austenite on the worn surfaces, experimental results were hardly found to evidence any newly formed martensite. The only direct evidence of fresh martensite beneath worn surface was obtained by SEM observation of martensite-like morphology on an etched subsurface [17]. On the other hand, TEM observations of worn surfaces confirmed that sliding wear caused nano-twinning deformation of retained austenite and greatly refined grains [37–39]. In another recent research paper, the authors reported that austenite in a Q–P treated steel did not transformed to martensite when the applied wear load was low [40].

In current work, comparative XRD analysis between worn surface and bulk material of the austempered steel confirms significant decrease of retained austenite, especially the blocky austenite, Fig. 15. In other words, the XRD work has confirmed that some retained austenite survived in the abrasive wear without transforming to ferritic structure. Nevertheless, this finding supports the positive role of retained austenite in facilitating the shear deformation. Indeed, shear deformation took place not only on the worn surfaces of austenite-containing samples, but also on those of all the other samples. The measured worn surface strain-hardening in the austempered samples was not outstanding as compared to other samples. In contrast, the martensitic samples showed even stronger strain-hardening than the austempered samples. Cross-sectional SEM observations also revealed that the microstructure in the top worn surface, in a depth less than 1 μm, was extremely disordered by the dynamic mixing of the abrasive wear. Considering the severe shearing deformation and anticipation of the frictional thermal energy in the extremely thin layer, it was unlikely to form typical tetragonal martensite. It is necessary to plan more detailed experimental study of the wear induced microstructure changes, e.g. to clarify the evolution of the retained austenite in the extremely thin top worn surface layer. Nevertheless, the role of retained austenite has been very positive in bringing in low friction and low abrasive wear.

5 Conclusions

Austempering treatments were applied on a medium-carbon low-alloy steel at its Ms temperature of 285 °C for various short holding times from 10 to 60 min. The two-body abrasive wear tests against a SiC abrasive disc were undertaken to investigate the wear properties and wear mechanisms as compared to those of martensitic and ferritic steels. The following conclusions have been made.

(1) Austempering by 10 min led to multi-constituent microstructure of nano-width bainitic ferrite, martensite and retained austenite. The short-term austempering helped refine the microstructure by intersecting the austenite grains, maintain comparable hardness property and gain superior wear resistance to the as-quenched martensitic sample.

(2) Further increase of austempering time up to 60 min resulted in microstructure of bainitic ferrite and retained austenite with more pronounced carbon partitioning. Despite its lower hardness of 5.6 GPa as compared to 6.7 GPa of the water-quenched martensitic steel, the steel austempered by 30 or 60 min possesses the best wear resistance.

(3) Micro-cutting and ploughing deformation were found to be the major wear mechanisms. The lower wear coefficient of the austempered samples was associated with their remarkably lower friction than the quenched sample. The superior wear and friction properties have been found to be attributed to the good plasticity of the austenite constituent in the austempered samples.

References

1. A.L. Roitburd, G.V. Kurdjumov, Mater. Sci. Eng. **39**, 141 (1979)
2. G. Krauss, Mater. Sci. Eng. A **273–275**, 40 (1999)
3. M. Kang, M. Zhu, Acta Metall. Sin. **41**, 673 (2005)
4. J.G. Speer, D.V. Edmonds, F.C. Rizzo, D.K. Matlock, Curr. Opin. Solid St. M. **8**, 219 (2004)
5. D.V. Edmonds, K. He, F.C. Rizzo, B.C. De Cooman, D.K. Matlock, J.G. Speer, Mater. Sci. Eng. A **438–440**, 25 (2006)
6. K. Zhang, W.Z. Xu, Z.H. Guo, Y.H. Rong, M.Q. Wang, H. Dong, Acta Metall. Sin. **47**, 489 (2011)
7. Y. Tomita, Int. Mater. Rev. **45**, 27 (2000)
8. M. Kang, Y. Yang, X. Zhang, J. Sun, H. Jia, H. Wu, Acta Metall. Sin. **32**, 897 (1996)
9. Z.G. Yang, H.S. Fang, Curr. Opin. Solid St. M. **9**, 277 (2005)
10. F.B. Yang, B.Z. Bai, D.Y. Liu, K.D. Chang, D.Y. Wei, H.S. Fang, Acta Metall. Sin. **40**, 296 (2004)
11. F.G. Caballero, H.K.D.H. Bhadeshia, K.J.A. Mawell, D.G. Jones, P. Brown, Mater. Sci. Tech. **18**, 279 (2002)
12. T.S. Wang, X.Y. Li, F.C. Zhang, Y.Z. Zheng, Mater. Sci. Eng. A **438–440**, 1124 (2006)
13. J. Yang, T.S. Wang, B. Zhang, J. Yanshan Univ. **35**, 427 (2011)
14. F.G. Caballero, M.K. Miller, A.J. Clarke, C. Garcia-Mateo, Scripta Mater. **63**, 442 (2010)
15. C. Wang, X. Li, Y. Chang, S. Han, H. Dong, Wear **362–363**, 121 (2016)
16. X.L. Xu, Z.W. Yu, Y.Q. Ma, X. Wang, Y.Q. Shi, Mater. Sci. Tech. **18**, 1561 (2002)
17. R. Colaco, R. Vilar, Wear **258**, 225 (2005)
18. S. Balos, D. Rajnovic, M. Dramicanin, D. Labus, O. Eric-Cekic, J. Grbovic-Novakovic, L. Sidjanin, Int. J. Cast Metal. Res. **29**, 187 (2016)
19. S.D. Bakshi, D. Sinha, S.G. Ghowdhury, V.V. Mahashabde, Wear **394–395**, 217 (2018)
20. S.D. Bakshi, P.H. Shipway, H.K.D.H. Bhadeshia, Wear **308**, 46 (2013)
21. M. Shah, S.D. Bakshi, Wear **402–403**, 207 (2018)
22. X.Y. Long, F.C. Zhang, J. Kang, Z.N. Yang, D.D. Wu, K.M. Wu, G.H. Zhang, Mater. Sci. Tech. **33**, 615 (2017)
23. W. Wang, R. Song, S. Peng, Z. Pei, Mater. Design **105**, 96 (2016)
24. F. Hu, K.M. Wu, P.D. Hodgson, Mater. Sci. Tech. **32**, 40 (2016)
25. S.D. Bakshi, A. Leiro, B. Prakash, H.K.D.H. Bhadeshia, Wear **316**, 70 (2014)
26. K. Abbaszadeh, H. Saghafian, S. Kheirandish, J. Mater. Sci. Technol. **28**, 336 (2012)
27. Q. Luo, M. Kitchen, V. Patel, M. Filleul, D. Owens, in *Proceedings HSLA Steels 2015, Microalloying 2015 and Offshore Engineering Steels 2015*, ed. by The Chinese Society for Metals (CSM). Hangzhou, November 11–13, 2015 (Springer, Cham, 2016), pp. 433–438
28. Q. Luo, M. Kitchen, S. Abubakri, Metals **7**, 258 (2017)
29. Y. Tomita, T. Okawa, Mater. Sci. Tech. **11**, 245 (1995)
30. Q. Luo, Lubricants **6**, 58 (2018)
31. Q. Luo, J. Mater. Eng. Perform. **25**, 2170 (2016)
32. C. Zhang, S. Li, D. Yi, W. Qin, H. Fu, J. Mater. Eng. Perform. **29**, 2460 (2020)
33. E.A. Badawi, M.A. Abdel-Rahman, A. Mostafa, M. Abdel-Rahman, Appl. Phys. **2**, 1 (2019)
34. H. Guo, A. Zhao, C. Zhi, R. Ding, J. Wang, Mater. Sci. Tech. **33**, 893 (2017). https://doi.org/10.1080/02670836.2016.1245239
35. A.M. Gola, M. Ghadamgahi, S.W. Ooi, Wear **376–377**, 975 (2017)

36. B. Narayanaswamy, P. Hodgson, I. Timokhina, H. Beladi, Metall. Mater. Trans. A **47**, 4883 (2016)
37. F. Katsuki, Wear **303**, 92 (2013)
38. B. Liu, X. Lu, W. Li, X. Jin, Wear **398–399**, 22 (2018)
39. C. Zheng, B. Lv, F. Zhang, Z. Yang, J. Kang, L. She, T. Wang, Scripta Mater. **114**, 13 (2016)
40. J. Yang, Y. Jiang, J. Gu, Z. Guo, H. Chen, Acta Metall. Sin. **54**, 21 (2018)